
This is an electronic reprint of the original article.
This reprint may differ from the original in pagination and typographic detail.

Lemstrom, Ida; Polojarvi, Arttu; Puolakka, Otto; Tuhkuri, Jukka
Load distributions in the ice-structure interaction process in shallow water

Published in:
Ocean Engineering

DOI:
[10.1016/j.oceaneng.2022.111730](https://doi.org/10.1016/j.oceaneng.2022.111730)

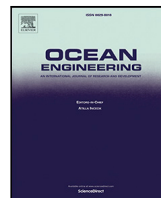
Published: 15/08/2022

Document Version
Publisher's PDF, also known as Version of record

Published under the following license:
CC BY

Please cite the original version:
Lemstrom, I., Polojarvi, A., Puolakka, O., & Tuhkuri, J. (2022). Load distributions in the ice-structure interaction process in shallow water. *Ocean Engineering*, 258, Article 111730.
<https://doi.org/10.1016/j.oceaneng.2022.111730>

This material is protected by copyright and other intellectual property rights, and duplication or sale of all or part of any of the repository collections is not permitted, except that material may be duplicated by you for your research use or educational purposes in electronic or print form. You must obtain permission for any other use. Electronic or print copies may not be offered, whether for sale or otherwise to anyone who is not an authorised user.



Load distributions in the ice-structure interaction process in shallow water

Ida Lemström^{*}, Arttu Polojärvi, Otto Puolakka, Jukka Tuhkuri

Aalto University, School of Engineering, Department of Mechanical Engineering, P.O. Box 14300, FI-00076 Aalto, Finland

ARTICLE INFO

Keywords:

Ice-structure interaction
Ice load
Ice load distribution
Model-scale experiments
Offshore structures

ABSTRACT

Model-scale experiments were performed to explore the process of level ice interacting with a, in model-scale, ten-meter-wide inclined structure in shallow water. During each experiment, an initially intact ice sheet was pushed against the sloping structure, failed against it and accumulated into a grounded rubble pile in front of it. The strength of the model ice used in the experiments was varied. The spatial and temporal ice load distributions were measured at two scales: the structure was divided into ten identical segments along its waterline with the horizontal load on each segment measured, while the local pressure distributions were simultaneously measured with tactile sensors from two of the segments. This paper focuses on the relationships between the loads on different segments and the correlation between global and local loads. The load records of the individual segments during the whole experiment correlated with each other. The Pearson correlation coefficient for the load records of two neighboring segments was about 0.8, and for segments having a distance of 5 m or more, about 0.4. The magnitudes of both the maximum and the mean load on each segment were approximately equal. Even if the segment loads correlated during the whole experiment, the load records of the individual segments showed also transient ice load peaks, which did not correlate. These were used to define local peak load events and related local line loads, defined by dividing the magnitude of a peak load by its width in space. Roughly 2/3 of the local peak load events concentrated on one segment and only about 5% of them covered more than three segments. Narrow local peak load events caused the local line loads of the highest magnitude, with the magnitude and the relative frequency of the events increasing with the ice strength. Narrow events resulted in local line loads up to four times higher than the global line load, which was defined by dividing the total load on the structure by its width. The investigation of the local peak load events also showed that an inclined structure having a width of approximately 5 m (the ice thickness to structure width ratio of 1:100) appeared infinitely wide and gave similar results as a wider structure. Ice pressure measurements showed a line-like pressure distribution at the waterline of the structure with the weakest ice, whereas with stronger ice, zones of high ice pressure were observed at upper parts of the segments.

1. Introduction

Human activities in ice-covered sea areas increase constantly. Optimizing the design of offshore structures still requires new engineering insight into various topics related to the ice loads on them. One important topic is the spatial distribution of ice loads and pressures during an ice-structure interaction process, with earlier full- and laboratory-scale measurements in the case of inclined structures being scarce. Timco (1991) performed laboratory-scale experiments to measure the vertical pressure distribution on a structure, where the loads on a segmented inclined structure were measured. The inclination angle of the structure was varied in the range of $\pm 30^\circ$ in relation to vertical. The results showed that even with a large rubble pile in front of the structure, a major part of the ice load is transmitted close to the waterline

of the structure. A similar load distribution was found by Tripathi et al. (2011), who examined the vertical and horizontal ice pressure distribution measured with tactile sensors from a conical portion of a pier of the Confederation Bridge. In contrast to this, Lu et al. (2013) used horizontal and vertical tactile sensor data from model-scale experiments on a downward sloping structure and found that the loads below the waterline were about equal in magnitude to those measured at the waterline. Other studies on ice load and pressure distributions have focused on ice crushing against vertical structures (Sodhi, 1998; Daley et al., 1998; Sodhi, 2001; Fransson, 2001; Jordaan, 2001; Riska et al., 2002; Frederking, 2004; Määttänen et al., 2011, 2012; Hyun-wook et al., 2018). Other types of laboratory-scale experiments on shallow water ice-structure interaction have previously been performed

^{*} Corresponding author.

E-mail address: ida.lemstrom@aalto.fi (I. Lemström).

<https://doi.org/10.1016/j.oceaneng.2022.111730>

Received 9 February 2022; Received in revised form 8 June 2022; Accepted 9 June 2022

Available online 21 June 2022

0029-8018/© 2022 The Author(s). Published by Elsevier Ltd. This is an open access article under the CC BY license (<http://creativecommons.org/licenses/by/4.0/>).

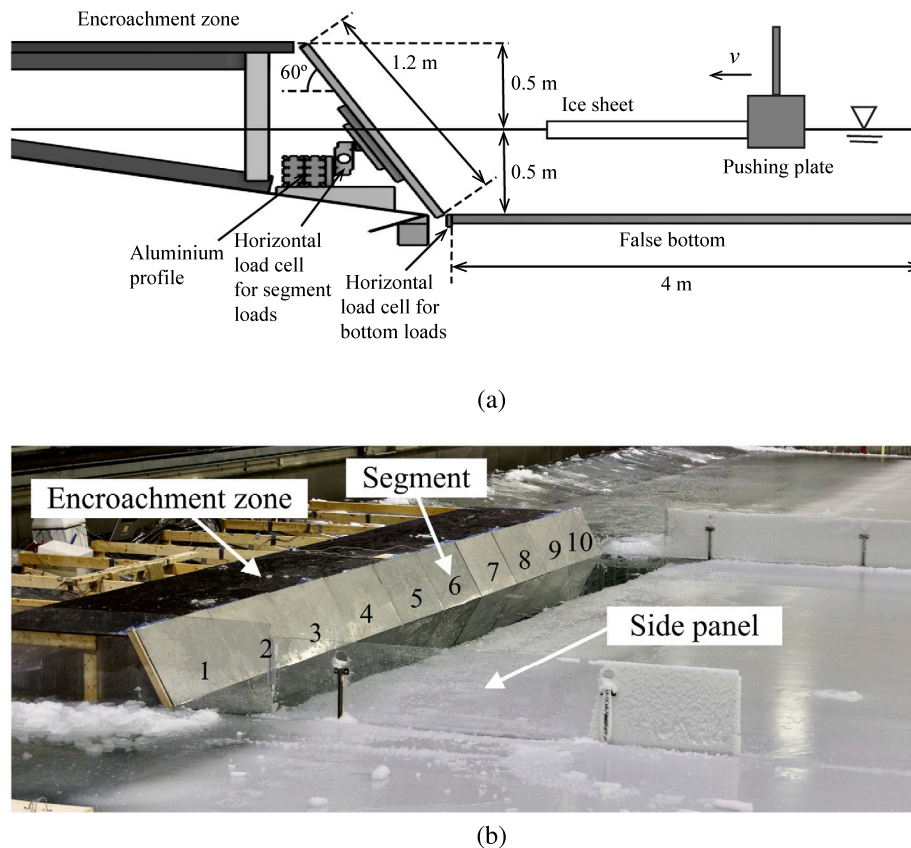


Fig. 1. Experimental set-up: (a) main dimensions and instrumentation and (b) general overview. The segment numbering 1...10 used in the text runs from left to right in (b). Source: Figure reproduced from Lemström et al. (2022).

by several authors (Yoshimura and Inoue, 1985; Timco et al., 1989; Karulin et al., 2007; Evers and Wehrauch, 2004; Repetto-Llamarez et al., 2009; Repetto-Llamarezrepe et al., 2009; Bridges et al., 2016, 2019) as discussed by Lemström et al. (2022).

As described above, only few model-scale tests on ice load distributions of inclined structures have been conducted before and none of them have considered shallow water and rubble pile grounding. Except for Bridges et al. (2016, 2019), who performed model-scale tests on a 5 m wide structure, the structure in previous shallow water experiments have not exceeded a width of 1.5 m (Lemström et al., 2022). Further, all of the earlier laboratory-scale experiments related to ice load distributions on inclined structures were conducted on structures having widths below one meter. No reported work, where the ice loading process on inclined structures have been studied on different widths or where the ice loads have been measured in different resolutions, exists. A deeper knowledge on the ice load distributions on inclined structures may give new tools for optimizing offshore structures, for designing future experiments, and for developing numerical simulations.

This paper studies ice load distributions in laboratory-scale experiments on the ice-structure interaction process in shallow water. In the experiments, an initially intact ice sheet was pushed against a ten-meter-wide inclined structure with a constant velocity. The ice rubble pile forming in front of the structure during the process reached the bottom, or in other words, the rubble pile grounded. The ice loads were simultaneously measured in two resolutions. The structure consisted of ten identical one-meter-wide segments and the horizontal load on each of these segments was measured independently with load cells (Fig. 1). Furthermore, the ice pressure on two of the segments was measured with tactile sensors. The campaign consisted of seven experiments in three test series with varying ice strength. In one of the series the compressive and flexural strength of ice was ~ 50 kPa; in the two other series, the ice was two and four times stronger.

The novelty of the experimental set-up used here lies within the segmentation of the structure and in the simultaneous load measurements performed in different resolutions. The segmentation of the structure allowed to study the correlation between the ice loads measured on the segments and to define a width for individual local peak ice load events. The relationship between global and local ice loads has always been a challenge for Arctic engineering, but is important for optimizing offshore structures. By identifying the local peak ice load events, this paper attempts to estimate the ratio between the global and local ice load on an inclined structure. Further, the local peak ice load events could be used to estimate a limit width, above which the structure could be considered infinitely wide. This limit is important for designing future model-scale experiments and simulations, yet it is rarely estimated. In addition to the horizontal segmentation of the structure, both the horizontal and vertical ice load distributions in the model-scale experiments were measured with tactile sensors. From this aspect, the experiments are more thorough than in any of the previously reported studies. Furthermore, by systematically varying the ice strength, its effect on ice load distributions was examined. This is important, since the ice strength has a clear effect on the global ice load levels and on the morphology of the ice rubble pile forming during the interaction process. This was shown by Lemström et al. (2022) by using the same set of experiments as here. It is, thus, justified to assume that the ice strength may influence the ice load distributions as well.

The paper is organized as follows. In Section 2, the experimental set-up, procedure and parameters are introduced. Section 3 presents the results from the experiments. Section 4 focuses on the analysis of the results and compares the work with earlier studies, and Section 5 concludes the paper. The paper continues a study by Lemström et al. (2022), who discussed the global ice load levels, the effect of ice strength on the global ice load, and the mechanical phenomena during the ice loading process.

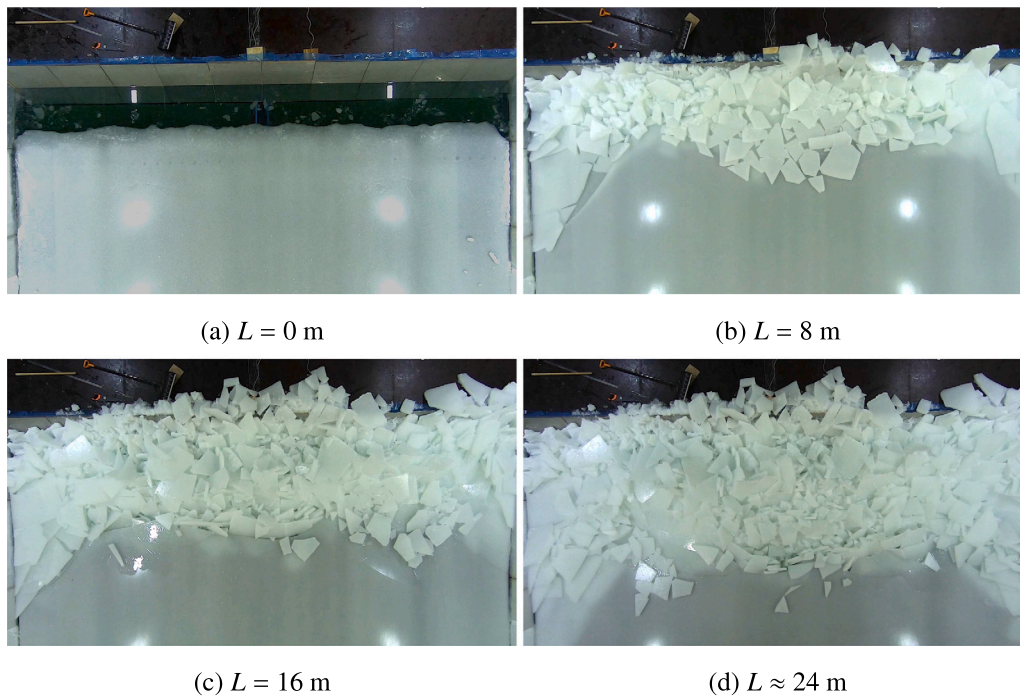


Fig. 2. Snapshots of the rubble pile-up process captured by the top view camera during experiment M-2, when 0, 8, 16 and approximately 24 m of ice has been pushed against the structure.

2. Experimental set-up

The experiments of this paper were performed in the Aalto Ice Tank ice test basin (Fig. 2). The experimental set-up, presented in Fig. 1a–b, is described in detail by Lemström et al. (2022). The experiments were performed by pushing a ten-meter-wide ice sheet against a sloping structure of the same width with a constant velocity of 50 mm/s (Fig. 2). The structure consisted of ten identical 1 m × 1 m (width × height) segments, it had an inclination angle of 60° and a freeboard of 0.5 m. The entire experimental set-up was sufficiently stiff for it to be considered rigid under the measured load. The structure was mounted on a fixed underwater ramp, and a separately supported 4-meter-long false bottom was positioned in front of it. The ice-structure and ice-bottom friction coefficients were measured to be approximately 0.1 and 0.5, respectively. The width of the segments was selected for practical reasons: As the structure was designed to be as wide as practically achievable, very narrow segments would have made the experiments very challenging to set-up and perform. Many of the test parameters, such as width and inclination angle of the structure, velocity of the ice sheet and ice thickness, were chosen together with industrial representatives to be typical for ice barriers in shallow water areas. During the experiments, the horizontal load on each segment was measured independently by a uni-axial single-point load cell. The structure was confined in between two vertical plexi-glass side panels, restricting the ice from moving around the structure, to mimic a two-dimensional ice accumulation scenario.

Segments 5 and 6 in the middle of the structure were instrumented with Tekscan #5400N tactile sensors to measure the local ice pressures. (The segments were numbered from one to ten according to Fig. 1b.) The sensors had a size 0.88 m × 0.58 m (width × height) and they consisted of 52 rows and 34 columns of sensels, each having an area of 17 mm × 17 mm. The tactile sensors were mounted in the center of the segments, and faced with sheets of 1 mm thick stainless steel to prevent direct contact with ice or water. Each sensor reached about 0.29 m below and above the waterline as measured along the inclined structure and covered about 43% of the segment area. The load values measured by the sensors may include some error and, thus, the measured pressure

Table 1

Ice properties in the seven experiments. H_i is the ice thickness, σ_f is the flexural strength of the ice, σ_c is the compressive strength of the ice and E is the elastic modulus.

ID	H_i [mm]	σ_f [kPa]	σ_c [kPa]	E [MPa]
W-1	50	44	46	107
W-2	52	50	51	112
W-3	52	42	54	103
M-1	50	109	121	387
M-2	51	108	130	328
S-1	52	211	214	2023
S-2	52	197	261	1529

values should be treated as relative. The reliability of the tactile sensor measurements is assessed in Appendix.

Table 1 presents the values of ice thickness, H_i , flexural strength, σ_f , compressive strength, σ_c and elastic modulus, E , for each of the seven experiments conducted. The experiments were performed in three test series: W, M and S. The experiments in series W, referred to as ‘weak’, were conducted with ice with the flexural and compressive strength of ~ 50 kPa, whereas the experiments in series M and S, referred to as ‘medium’ and ‘strong’, were conducted with ice having target flexural and compressive strengths of two and four times higher than the ice in series W, respectively. The ice strength was systematically varied between the strength of the typical model-scale ice of the Aalto Ice Tank and the strongest ice that the current test fixtures withstand. To obtain concrete results and to make analysis of the results straightforward, the number of varied variables in the test campaign was kept limited. The measurements of the ice properties are presented in detail by Lemström et al. (2022). Due to technical problems, tactile sensor measurements were only available for experiments W-2, M-2 and for segment 6 of M-1.

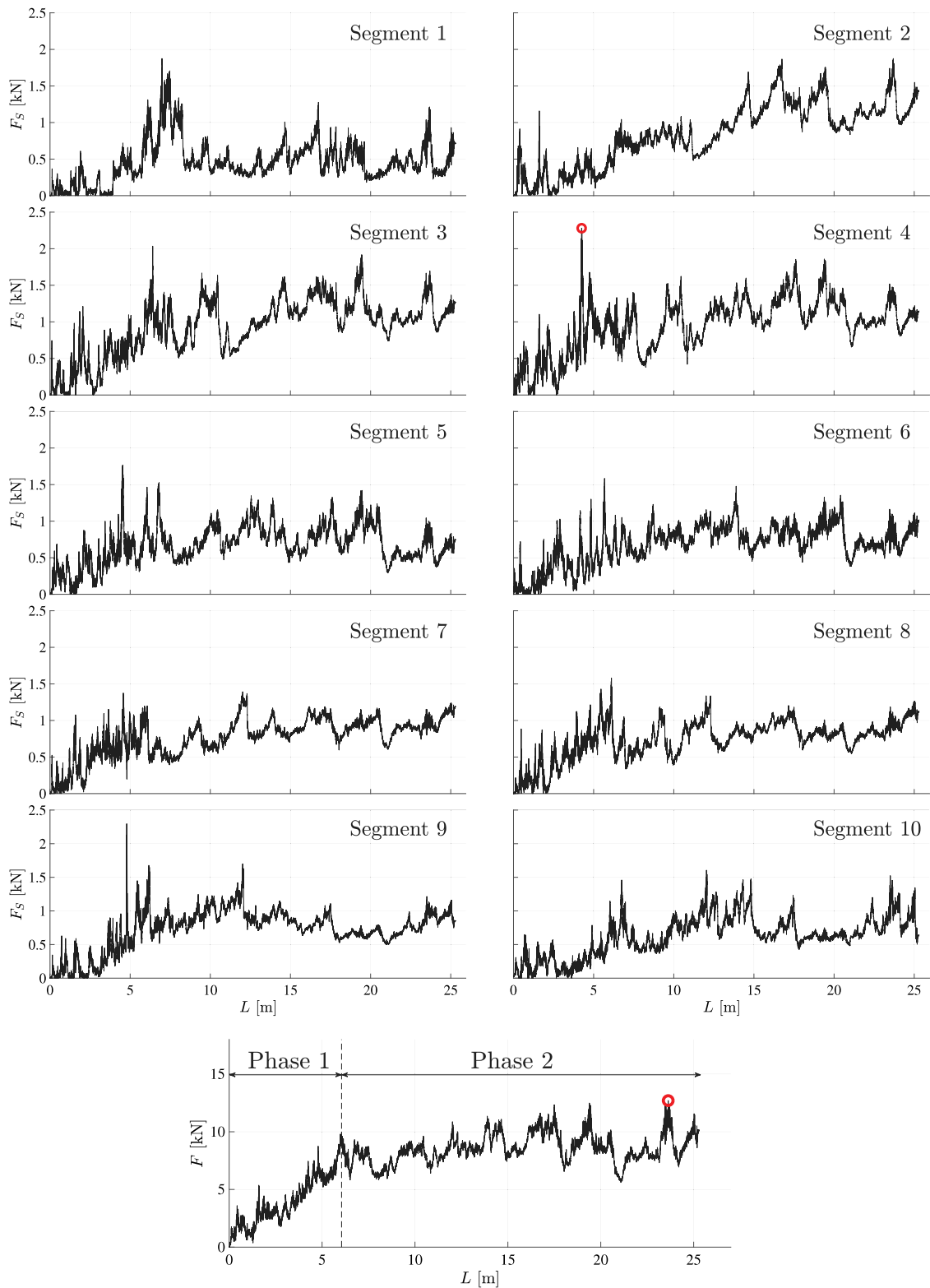


Fig. 3. The horizontal segment ice load, F_S , measured from each of the ten segments in experiment M-1, and the horizontal global load, F , as a function of the length of ice pushed against the structure, L . The first, linearly increasing and the second, steady-state phase of the global load record, as well as the peak global load, are illustrated in the undermost figure. The load peak indicated in the load record of segment 4 will be addressed in Section 4.2.

3. Results

3.1. Segment loads

Fig. 3 shows the horizontal ice load, F_S , on each segment and the horizontal global load, F , taken as the sum of the loads on each of

the ten individual segments, as a function of the length, L , of the ice pushed against the structure in experiment M-1. All $F_S - L$ records showed the same general level features: First F_S increased, after which a steady-state phase with a more or less constant load was reached. The two distinct phases are illustrated in the undermost figure. The phases were observed even more clearly in the global load records

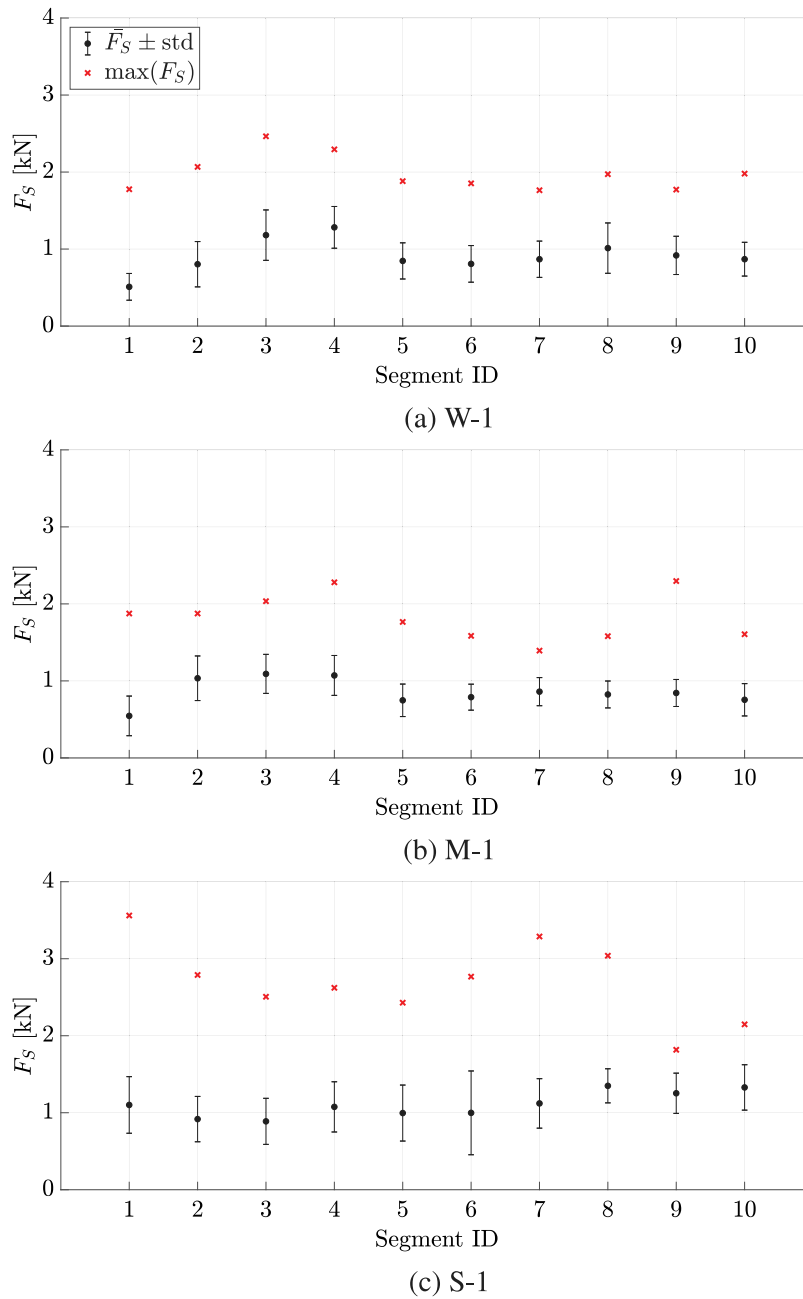


Fig. 4. The mean ice load, \bar{F}_S , the standard deviation and the peak ice load, $\max(F_S)$, for each of the 10 segments during experiment (a) W-1, (b) M-1 and (c) S-1. Only the second, steady-state phase of the load records were considered when establishing \bar{F}_S . The segments are numbered from left to right in Fig. 1b.

from all experiments (Lemström et al., 2022). Due to the segment-to-segment variation, the two phases and the beginning of the steady-state phase are not as distinct in the segment load records as in the global load records. This readily suggests that the ice load was not distributed evenly throughout the structure width. Fig. 3 further shows that F_S on segments close to the edges of the structure started to increase slightly later than on those in the middle of the structure, which is an indication of slight effect of boundaries on $F_S - L$ records.

Fig. 4 presents the mean of the segment load, \bar{F}_S , its standard deviation and the peak segment ice load, $\max(F_S)$, for each of the ten segments during an experiment in test series W, M and S. (The segments were numbered from one to ten starting from the left end of the structure as Fig. 1b shows.) The mean load and the standard deviation were determined by using the $F_S - L$ -records from the second, steady-state, phase of the experiments only. The breaking point between the first and the second phase of the experiments was determined visually and the

same breaking points as with the global load, presented in Lemström et al. (2022) were used.

Fig. 4 shows that the mean segment loads, \bar{F}_S , were almost constant throughout the width of the structure, indicating that the load records measured on the individual segments would correlate with each other. As expected, the figure also shows that the highest values of \bar{F}_S were measured with the strongest ice, but also, surprisingly, that higher loads were measured with the weak ice than with the medium ice. A similar observation applied to global loads, as reported in Lemström et al. (2022). On the other hand, the average $\max(F_S)$ in the experiment with medium ice was slightly higher than in the experiment with weak ice. This is the case even if the global peak load was higher with the weak ice than with medium ice. The global peak load typically occurred, when high loads were measured on several segments and its instance did not usually match the instance of peak load on any of the individual segments.

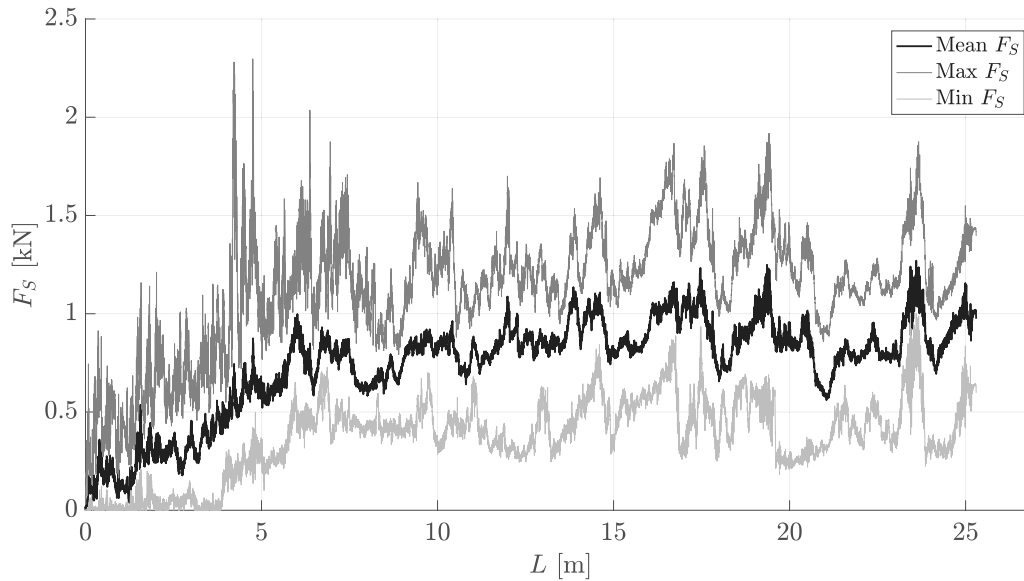


Fig. 5. The mean, maximum and minimum value of the segment load F_S , as functions of L , for experiment M-1.

Fig. 5 shows the mean, minimum and maximum for F_S during experiment M-1. The mean segment load refers here to the average of the ten segment loads at given L . Similarly, the smallest and largest load induced on a segment at given L is used as the minimum and maximum load, respectively. The mean, maximum and minimum segment loads appear to correlate strongly: Very often load peaks and drops in all three records occur simultaneously. The maximum load was approximately 50% larger than the mean load and the mean load approximately twice as large as the minimum load.

Fig. 5 further illustrates the differences in the segment load records during the first, linearly increasing phase. Interestingly, once the linearly increasing phase starts, the slope of the increase is equal (~ 1.5 kN/m (Lemström et al., 2022)) for the minimum, mean and maximum load; the first phase of the linearly increasing ice load seems to end at the same instance throughout the entire width of the structure. As Fig. 3 showed, the linearly increasing phase started later on in the process for the segments further away from the middle of the structure: The minimum segment load describes the loads on these segments rather well. The maximum loads, on the other hand, describe the loads on the segments located in the middle of the structure.

3.2. Local ice pressures

The local ice pressure values on segments 5 and 6 were measured using tactile sensors (Section 2). Fig. 6 shows the mean pressure, \bar{p}_{ij} , on each sensel of the sensor on segment 5 in experiments W-2 and M-2. In \bar{p}_{ij} , i and j stand for the sensor rows and columns, respectively. The \bar{p}_{ij} distributions are presented separately for the phase of linearly increasing ice load (Fig. 6a) and steady state phase of the process (Fig. 6b). The two distinct phases of experiment M-1 are illustrated in Fig. 3.

As Fig. 6a shows, the values of \bar{p}_{ij} during the first phase were low and distributed evenly underwater. During the second phase with weak ice (Fig. 6b), the high pressure values occurred mainly at the waterline. The pressure distribution during the second phase of the experiment with weak ice was line-like, but not continuous across the entire width of the segment. On the contrary, during the second phase of the experiment with medium ice, no high values of \bar{p}_{ij} were found at the waterline region or directly around it. Instead, high pressure zones were observed at the upper part of the tactile sensor, approximately 500 mm from the lower edge of the sensor. No clear change in the pressures below waterline is observed between the first and second phase with the medium ice.

The vertical pressure distribution and high pressure zones were studied in more detail, by looking into the vertical distribution of \bar{p}_{ij} . This was performed similarly to Tripathi et al. (2011). To obtain the vertical pressure distribution, the percentage of all \bar{p}_{ij} values exceeding a threshold value of 5 kPa on each sensor row, i , was calculated using

$$P_i = \frac{N_{p_i}}{N_i} \times 100 \quad [\%], \quad (1)$$

where N_{p_i} is the total number of threshold-exceeding pressure values on row i , and N_i the total number of threshold-exceeding pressure values recorded by the entire tactile sensor. (Results presented below were not sensitive to the chosen threshold value on range 0.5 kPa... 30 kPa tested).

Fig. 7a and b present the P_i -values for all 34 rows of the two tactile sensors in experiments W-2 and M-2, again separately for the two phases of the experiments. The figure confirms the observations made above: The high pressure values during the first phase of the process are mainly located below the waterline with both weak and medium ice. During the second phase, the high pressure values occurred mainly directly at the waterline when the ice was weak, but with the stronger ice, only very few high pressure values are measured at the waterline region. With the stronger ice, the loads are transmitted close to the top of the tactile sensor. With some small high pressure points scattered also below the waterline, the pressures in the case of the stronger ice seem to create a bi-modal pressure distribution. Thus, even if in this case the force resultant would be located at the waterline, only few high loads are induced at this area. In this case, lower resolution measurements for determining the location of the force resultant could incorrectly suggest that the ice load is transferred to the waterline.

4. Analysis and discussion

4.1. Correlation between segment loads

Results above suggest that the loads measured on the individual segments would correlate. To study this in more detail, the Pearson correlation coefficients, R , between the complete ice load records for all possible segment combinations were determined. The Pearson correlation coefficient measures the linear correlation between two data sets and has values varying between -1 and 1 , where 1 designates total positive correlation, 0 designates no correlation and -1 designates

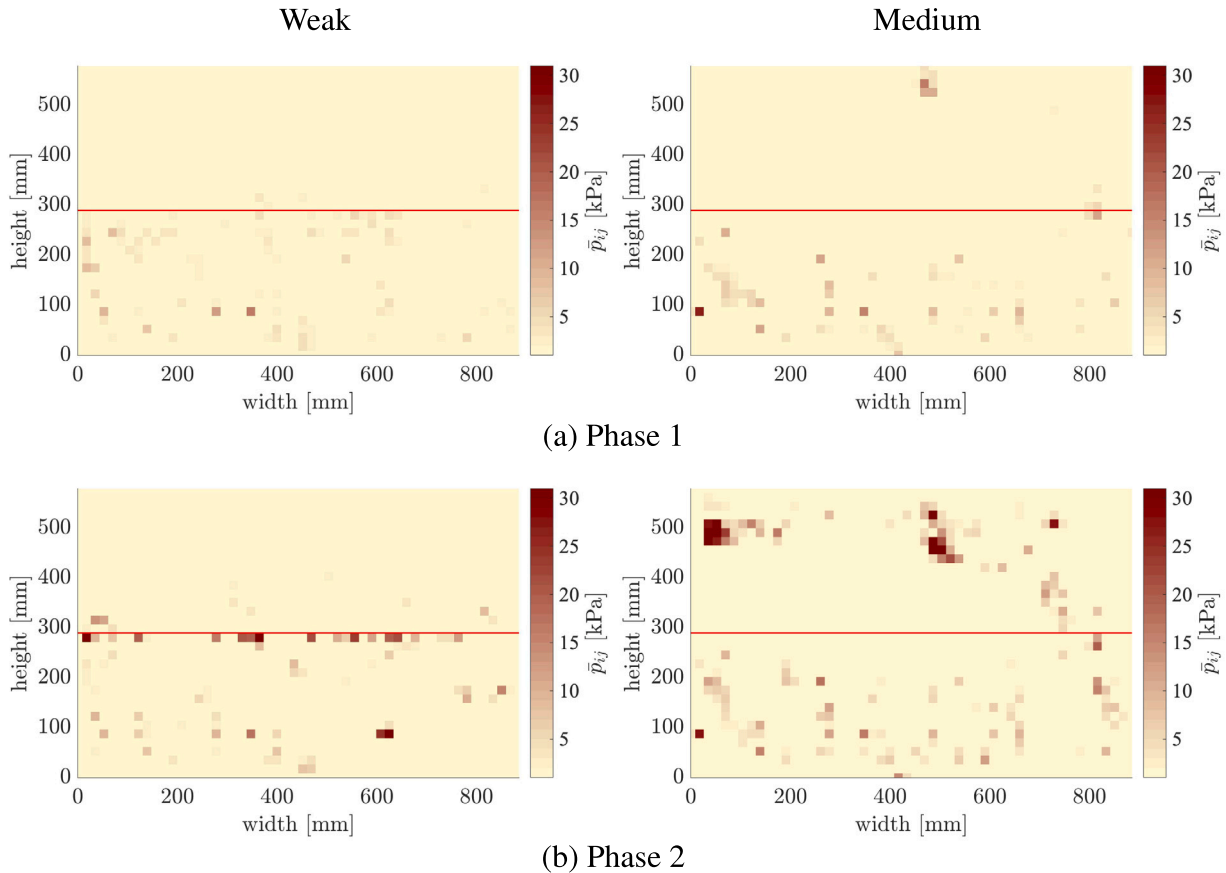


Fig. 6. The mean pressure distributions for the tactile sensor on segment 5 for the two phases of the ice loading process of experiments W-2 and M-2. The waterline is represented by a red line. The tactile sensors were located at the center of the 1 m wide and 1.2 m tall segment both in the horizontal and vertical direction. One pressure sensel has the area of 17 mm × 17 mm. The figures represent the entire area of the tactile sensor, located along the inclined structure.

total negative correlation. R is the ratio between the covariance of two variables and the product of their standard deviations:

$$R_{a,b} = \frac{\text{cov}(a,b)}{s_a s_b}, \quad (2)$$

where $\text{cov}(a,b)$ is the covariance between $F_S - L$ records a and b , and s_a and s_b are standard deviations of the records. The covariance is a measure of the relationship between two variables and evaluates to what extent the variables change together. In this paper, the following interpretation of the correlation coefficient values is used: Values of R above 0.7 signify a very strong correlation, values above 0.4 a strong correlation, values above 0.3 a moderate correlation, and values below 0.3 a weak or negligible correlation.

Fig. 8 presents the correlation coefficients for all possible segment combinations as a function of the distance between the segments (the distance between two neighboring segments is 1 m and the distance between the outermost segments is 9 m). The figure shows the average correlation coefficient, \bar{R} , for each distance with red marker. The data from all experiments belonging to test series W, M and S are presented in **Fig. 8a–c**, respectively.

As **Fig. 8** shows, there is a strong correlation for most of the segment combinations during the entire experiment. R for the $F_S - L$ records of neighboring segments is about 0.8. As the distance between a pair of segments increases from 1 to 5 m, R decreases, as would be expected. However, as the distance increases further, R remains on a rather constant level of 0.4. Out of all segment combinations, about 54% had values of R between 0.4 and 0.7, which signified a strong correlation, whereas the share of the R values higher than 0.7 was 25%, which signified a very strong correlation. Only 21% of the R values were lower

than 0.4, which signified only a moderate or negligible correlation. **Fig. 8** also shows, that R during the entire experiment, is on an average up to about 15% higher with the strong ice than with the weak and medium ice.

Fig. 9 demonstrates how the correlation of the $F_S - L$ records developed during the experiments with weak and strong ice, respectively. The graphs show the values of \bar{R} for four L intervals, which are simply the four quarters of the total length of ice pushed against the structure, L_{max} . As the figure shows, all values of \bar{R} are in an approximate range of 0.4...0.6 during the first L interval, regardless of the ice strength. During this interval, \bar{R} is relatively high for all segment pairs since the ice goes through consecutive local bending failures in a uniform pattern along the width of the structure. After the first L interval, the values of \bar{R} significantly drop for the next two intervals. This decrease is potentially due to ice partially failing against the structure and partially against the ice rubble pile. During the last L interval, the values of \bar{R} appear to be relatively high, but decreasing with the distance. This indicates that the ice failure process becomes more local towards the end of the experiments when there is a rubble pile in front of the structure. During the last L interval, the ice fails completely against the rubble pile in front of the structure (Lemström et al., 2022).

The values of R were in the model-scale experiments found to be strongly influenced by the size of the area on which the load was measured. Thus, the presented values of R are valid for this experimental set-up only and should be treated as relative values, which indicate trends rather than absolute values. While there would be a need to establish a relationship between the correlation coefficient values and the area used in the load measurement, it is left for future work.

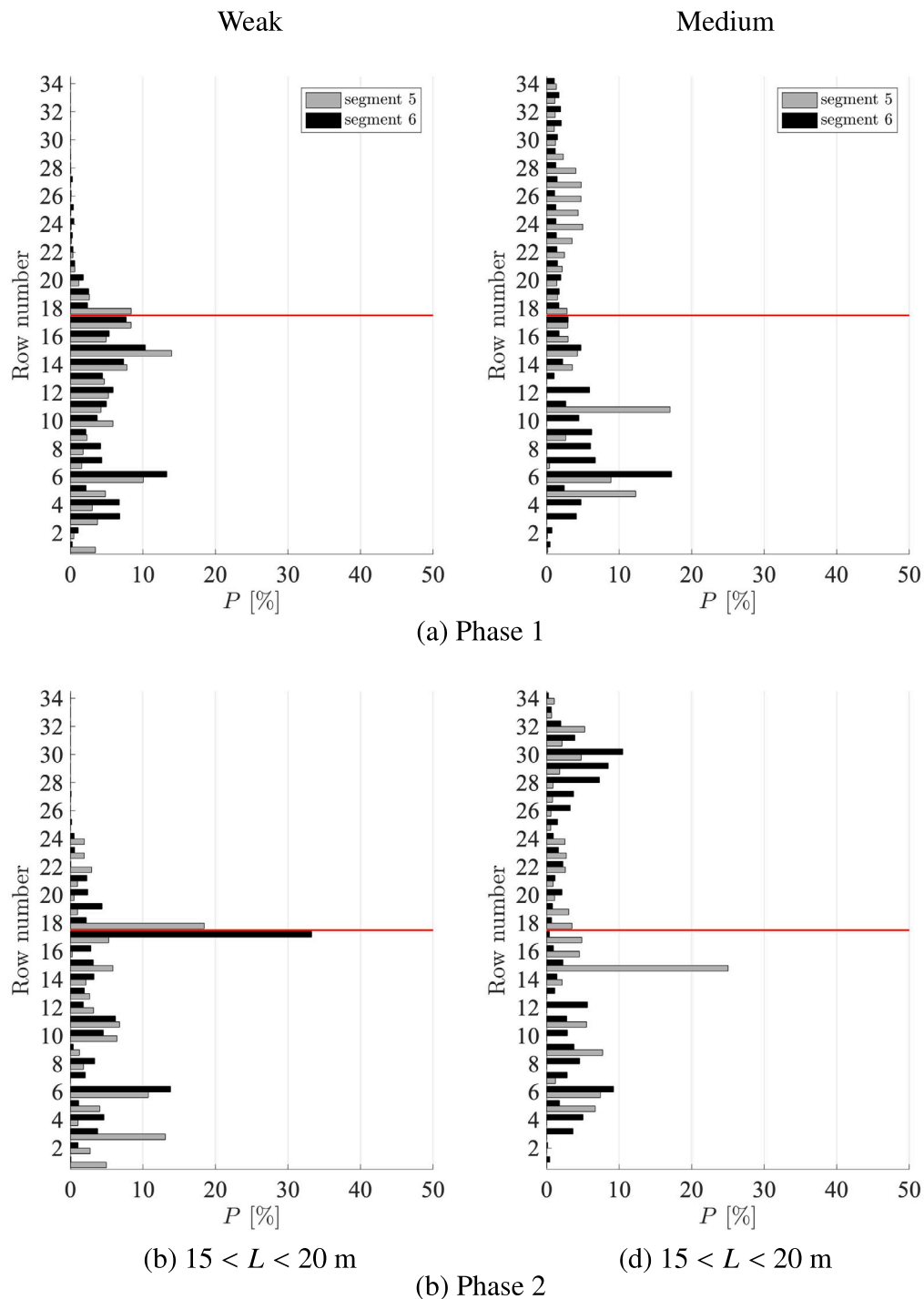


Fig. 7. The percentage of pressure values exceeding a threshold value of 5 kPa, P_i , for each of the 34 tactile sensor rows during the two phases of experiments W-2 and M-1. The results are shown for the two instrumented segments, 5 and 6, in the middle of the structure. The location of the waterline is marked with a red line. One row of the tactile sensor has the height 17 mm.

4.2. Local peak load events

Fig. 8 showed a strong correlation between the ten $F_S - L$ records measured in each experiment. Even if this was the case, the load peaks on the individual segments did not necessarily depend on each other. One such peak is indicated in the $F_S - L$ record of segment 4 in Fig. 3. The peak load in this case, reached a value of approximately 2.3 kN, about 50% of the global load measured at the same instance. For the short duration of this transient peak, the segment loads do not correlate; only the $F_S - L$ record of the neighboring segment 5 shows

a simultaneous peak of a lower value. It is clear that during the event described here, the ice load on the structure is not uniformly distributed but concentrated on segments 4 and 5.

The peak loads were used to define local peak load events, identified from the $F_S - L$ records by using Rayleigh separation, which is based on a comparison between the local minima and maxima within a load history. Two local maxima of F_S are considered to belong to two separate load events, if the local minimum F_S between them is smaller than the lower maximum multiplied by a separator constant. In addition, the higher value of the found local maxima must exceed a

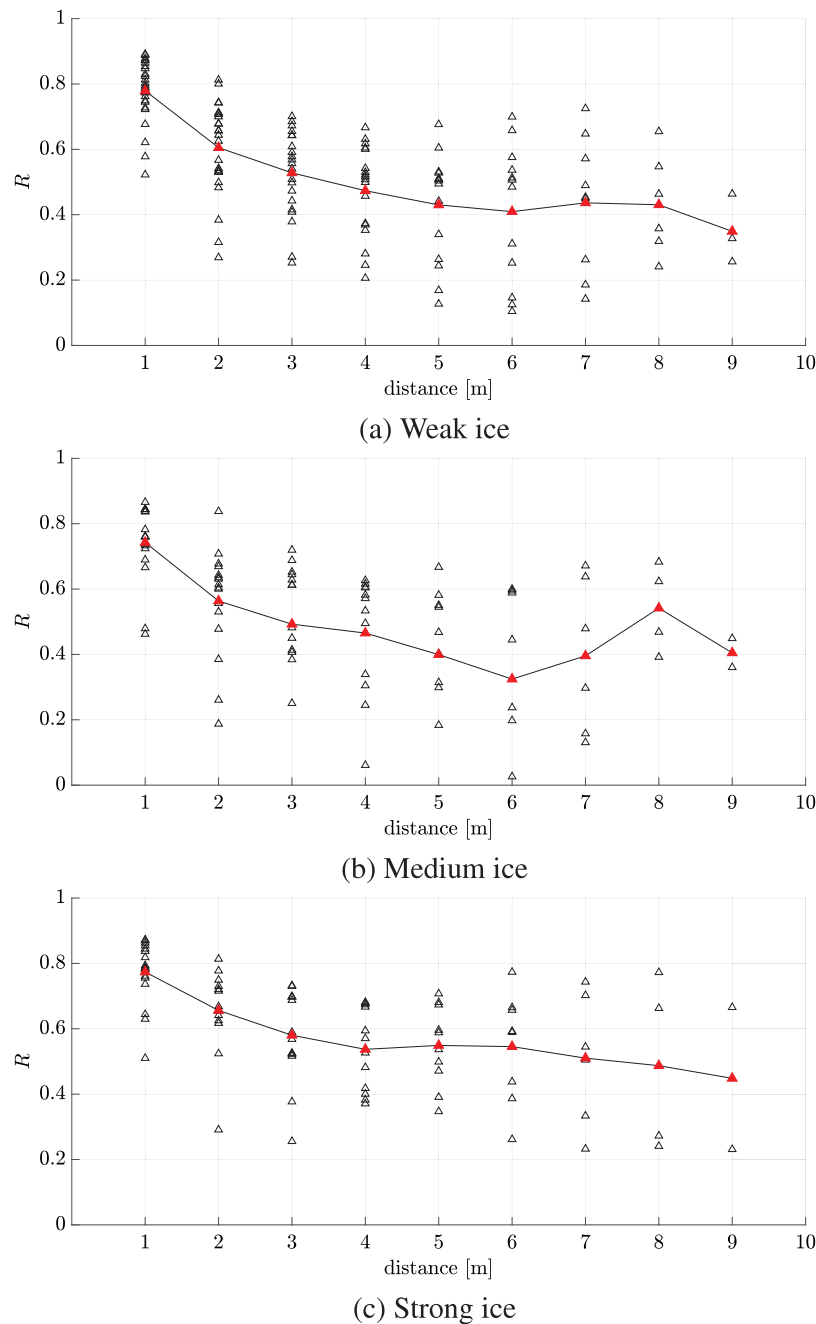


Fig. 8. Correlation coefficients, R , for the segment load, $F_S - L$, records. R values for all possible segment combinations as function of the distance between the segments is shown separately for test series (a) W, (b) M and (c) S. The distance is defined as the distance between the center points of the segments. R for all experiments in each test series are shown. The mean value for each distance is indicated with a red marker and the points are connected with lines.

chosen threshold value. Here the separation coefficient was chosen to be 0.5 and the threshold value 1000 N. The interval for a local peak load event was defined to start from the found local minimum and end to the local maximum following it. Fig. 10a shows an example of a local peak load event.

The peak load events were analyzed. The events for the analysis were chosen as follows: The $F_S - L$ records were divided into 20 one-meter-intervals and the peak with the highest maximum during the given interval was selected as the event for that interval. The load event width, B , was determined for the selected events according to how many adjacent segments fulfilled the two conditions illustrated in Fig. 10. The load event was defined to be distributed on two segments if: (1) The Pearson correlation coefficient, R , between the $F_S - L$ records of the segments for the duration of the event was > 0.75 and (2) the

value of F_S at the instance of the maximum load was > 0.75 times the magnitude of the maximum load, F_{max} . (The results were not sensitive to the chosen threshold values on the range 0.5...0.9 tested.) The chosen load events were generally short in duration. The total length of ice pushed against the structure during the load events averaged 0.9 m and the standard deviation was 1. During 70% of the load events, less than one meter of ice was pushed against the structure.

Fig. 11 shows a histogram for the values of B for weak, medium and strong ice. Most of the local peak load events were narrow, and the share of the narrow load events increased significantly with the ice strength. With strong ice, 75% of the load events concentrated on one segment only, whereas 47% and 65% of the load events with weak and medium ice had the width of one segment, respectively. Only about 5% of the load events covered more than three segments. This shows

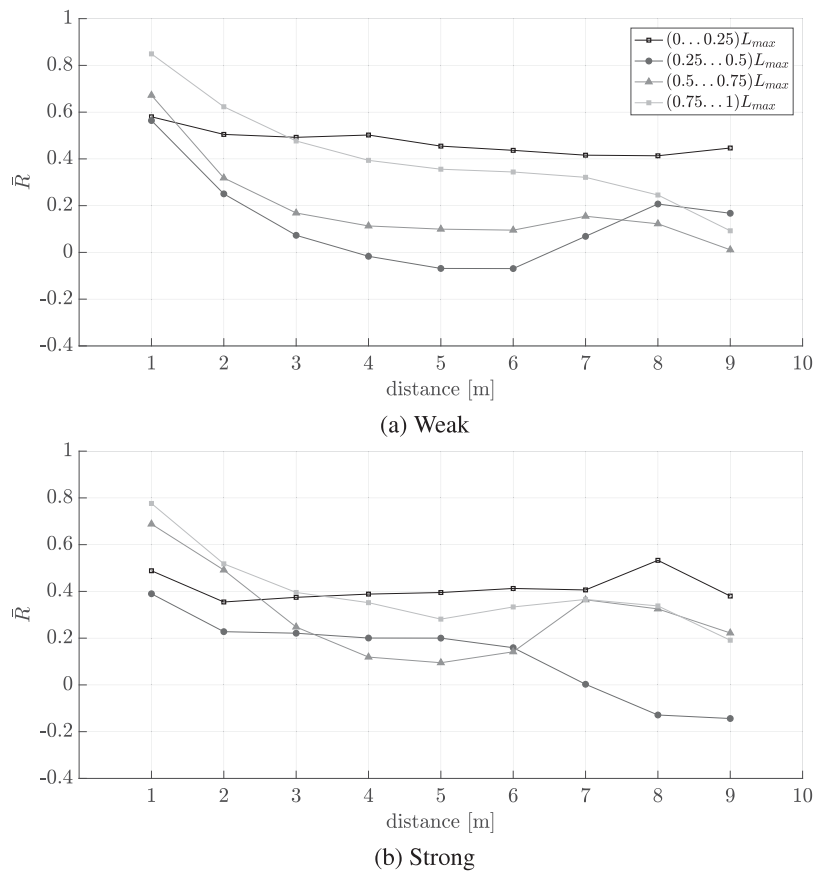


Fig. 9. The mean correlation coefficients, \bar{R} , as a function of the distance between the center points of the segments, given for four different intervals of the length of ice pushed against the structure, L . Figures (a) and (b) include the data from all experiments with weak and strong ice, respectively. The four intervals represent quarters of the total length of ice pushed against the structure, L_{max} , during each experiment.

that even if the $F_S - L$ records correlated for the entire experiment, the structure experienced high local peak loads, that did not relate to the overall correlation coefficient. Section 3.2 showed that the ice pressure distribution towards the end of the experiments with weak ice was line-like, whereas zones of high pressure were scattered around the segment with medium ice. This aligns with the finding that an increase in ice strength leads to narrower local peak load events, and, in fact, the scattered zones of high pressure suggest that the local peak loads were focused on an area narrower than one segment in the case of medium ice. The results of Fig. 11 are also in line with Suominen et al. (2017), who studied the width of ice loading during the level ice breaking process of a full-scale ship and found the cases with narrow loading to be more common than cases with wide loading.

To study if the load magnitudes during the peak load events show any scale effect, a local line load, q_l , was defined as the sum of the segment loads belonging to a given local peak load event divided by B of the event. Fig. 12a shows that the magnitude of q_l decreased as B increased; wide load events always yield local line loads small in magnitude, whereas narrow load events can result into high local line loads. Fig. 12a also shows that q_l increases with ice strength. It is interesting to notice that the medium ice yields q_l higher in magnitude than weak ice, even if higher global loads were measured for weak ice (Lemström et al., 2022).

Fig. 12b compares q_l to the global line load, q_g , at the instance of the load event maximum. The global line load, q_g , was defined by dividing the global ice load on the structure by the width of the structure. The figure shows that the values of q_l are often several times higher than the values of q_g : When the load event is narrow and the ice strong, q_l may reach values four times higher than q_g . For load events with $B > 1$ m, the q_l to q_g ratios are approximately equal for all ice types tested.

Overall, the q_l to q_g ratios of the figure show that local line loads cannot be calculated based on the global ice load only. Further challenges for estimating q_l arise from the fact that the global maximum load on the structure did not often occur simultaneously with the local peak load events (Fig. 3). Instead, when high global loads were measured, B was usually large and the magnitude of q_l low; the highest measured global load resulted to a line load of 2.2 kN/m (shown in Fig. 12a), one third of the highest magnitude of q_l . It was during the narrow load events, that the maximum values of q_l and F_S on the individual segments were reached (Fig. 12).

Interestingly, Fig. 12a and b indicate that a structure with a width of 4–5 m yielded similar line loads than a wider structure would. If $B < 4$ m, the values of the local line loads, q_l , exceed the global line load, q_g , measured for the entire ten-meter-wide structure, but if B is larger than about 4 m, q_l stays constant. Therefore, in these experiments, the structural width of 4–5 m, about 100 times the ice thickness, appeared infinite.

Finally, Fig. 13 illustrates how the load event width, B , increased with the length of pushed ice, L . At the initial part of the ice-structure interaction, when there is only a limited amount of rubble, the ice sheet fails directly against the structure. In this case the local load events appear to remain narrow. As the rubble pile in front of the structure grows, B increases, indicating that the load becomes more evenly distributed on the structure. No clear trend between the magnitude of the local line load, q_l , and the length of the ice pushed against the structure was observed.

The results of Section 4.1 indicated that the R values are high and thus, on average, the ice-structure interaction process shows similar phases along the width of the structure. The results here, however, showed that local peak load events, leading to occasional line loads of

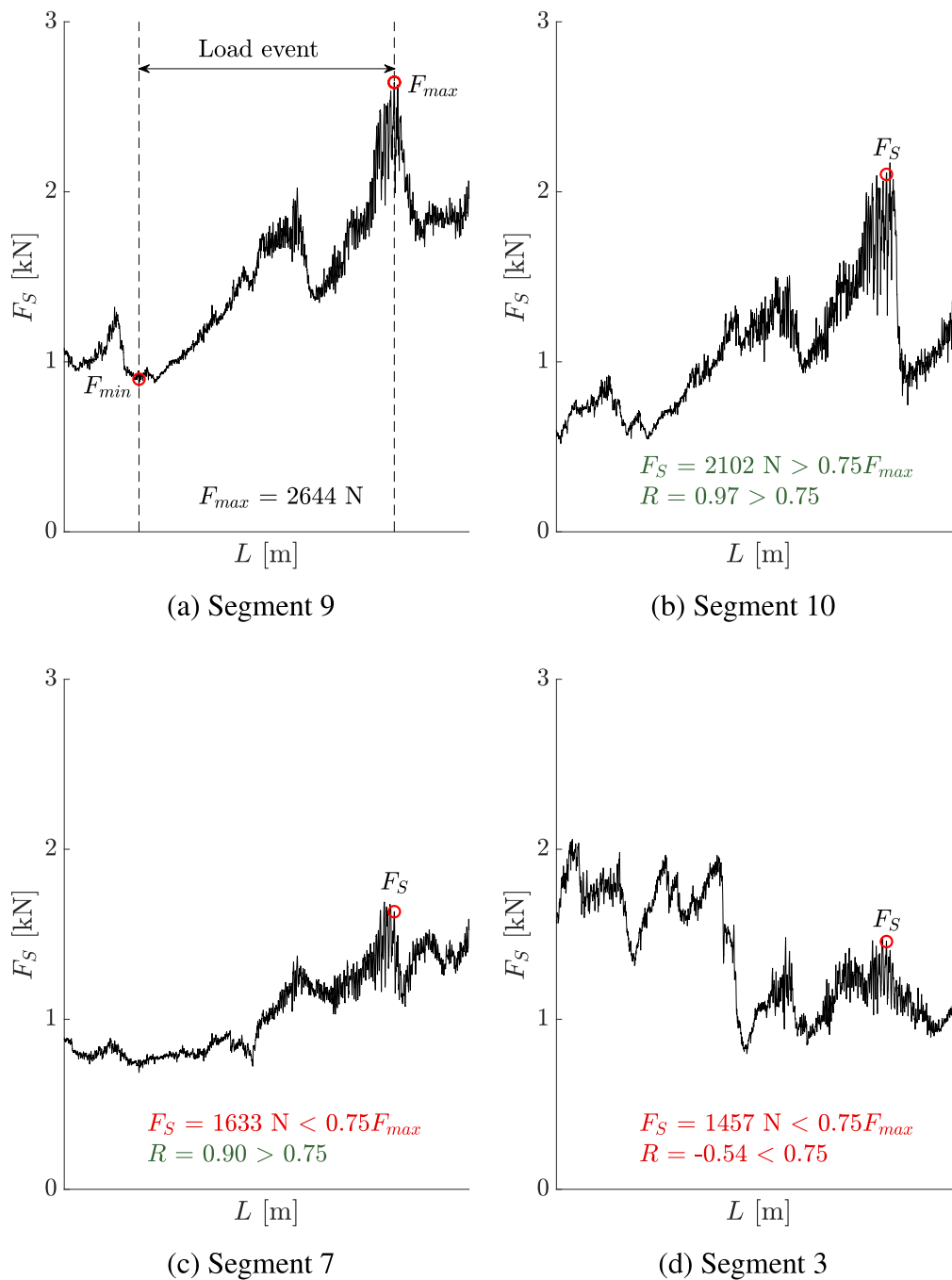


Fig. 10. Two segment load intervals belong to the same load event if: (1) The correlation coefficient, R , for the duration of the load event between the segments was > 0.75 and (2) the value of F_S at the instance of the maximum segment load, F_{max} , related to the event was > 0.75 times of it. Figure (a) shows the selected load event and the load maximum, F_{max} . The load interval of segment 10 (Figure b) fulfills both the criteria and belongs to the same load event, but the load intervals of segments 7 and 3 (Figures c and d), do not fulfill one or both criteria and belongs to separate load events.

high magnitude, are transient and, as such, do not affect the values of R . Both aspects are, however, important when interpreting the results. The maximum magnitudes of q_l may be essential when, for example, choosing material thickness for the structure. On the other hand, if the maximum magnitudes of q_l are used when calculating the maximum global load to, for example, design a foundation for a structure, overdimensioning is evident. For an optimal design, the maximum global and local line loads should be determined separately.

Ice model tests are frequently used to predict ice loads on offshore structures and ships. As a material, model-scale ice differs from sea ice, and it cannot simultaneously model all aspects of sea ice and its failure. However, since model-scale tests are less expensive, easier to

conduct, and allow a better control of variables than full-scale experiments, it is still the state-of-the-art method to gain new knowledge on phenomena related to the ice failure processes. Since model-scale ice cannot correctly reproduce every detail of the mechanical behavior of sea ice, dominating failure modes to be scaled correctly must be selected. These depend on the application. For example, during an ice-ship interaction process, the dominating ice failure mode is flexural failure, thus, the flexural strength is the primary ice property to be considered in scaling (Enkvist, 1972; Varsta and Riska, 1977; Valanto, 2001).

For the experiments here, the ice properties that needed to be scaled are not straightforward to define, as the interaction process consists of

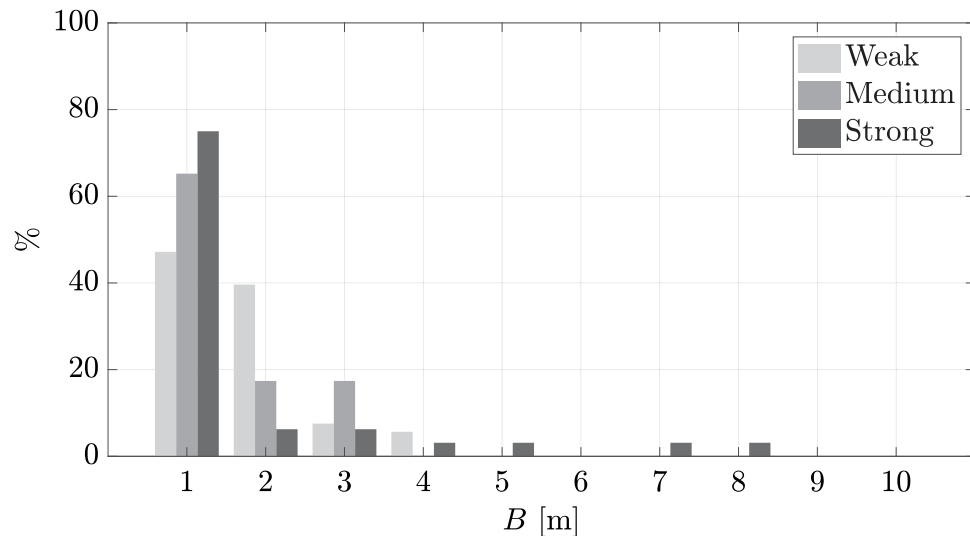


Fig. 11. Histogram for the local peak load event widths, B , with different ice types. B was here determined as described in the text.

two main phases (Lemström et al., 2022)—there is no one dominant failure mode for the whole process. The ice strength, however, was systematically varied to gain some insight on its effect on the loading process. At the start of the interaction process, the dominant failure mode was always flexural failure, which occurred against the structure. As more ice rubble had formed, the failure of the still intact sheet usually occurred inside the rubble pile and could not be visually detected. The dominant failure mode, however, had likely changed at this point, as buckling of large ice blocks could be identified from the under-water video footage. As described in Lemström et al. (2022), it was evident that the weak ice failed by crushing to a larger extent than the medium and the strong ice. This was clearly seen from the rubble piles after the experiments: The strong ice failed into distinct blocks, while a significant amount of crushed ice and slush was created as the weak ice failed. The interaction process in the experiments is similar to what have been observed in the field (Croasdale, 2011; Palmer and Croasdale, 2013), as discussed in more detail in Lemström et al. (2022).

The scaling related to the experiments is discussed further in Lemström et al. (2022), but it is not straightforward. The purpose of this paper is not to address scaling. We, however, believe that analogous effects and phenomena as discussed here would also be relevant in full-scale.

4.3. Ice pressure distributions

The ice pressure distributions of Section 3.2 showed that the highest pressures for both the weak and the medium ice were measured below the waterline at the beginning of the interaction process. As more ice was pushed against the structure, and a rubble pile formed, the pressure distribution in the case of the weak ice appeared to be line-like and the high pressure values were found at the waterline. With the medium ice, no high pressures were observed close to the waterline, but instead, high pressure zones were found at the upper part of the tactile sensor. The reason for the difference in pressure distributions with the two ice types is likely in the morphology of the ice rubble piles. Since the interior of the rubble piles with weak ice consisted of a slush-like substance (Lemström et al., 2022), the forces from the still intact ice sheet were transmitted through the slushy rubble to the waterline of the structure. In the case of the medium ice, the forces were distributed on the structure according to the configuration of the ice blocks within the rubble. In brief, when the ice is strong enough to form a rubble pile consisting of ice blocks, the pressure distribution depends on how the ice blocks are located. This finding is supported by the observation that the highest pressure values did not change their location during

the second phase of the process. During the second phase, the ice failed against the rubble pile and not against the structure (Lemström et al., 2022) and, thus, the ice rubble blocks in contact with the structure stayed in place.

The results of this paper concerning weak ice agree with those of Timco (1991). Timco studied ice pressure distributions on a horizontally segmented inclined structure and found that for an upward sloping structure, the maximum ice load occurred in the waterline region of the structure. Further, the loads, further away from the waterline, were in general low. However, as Figs. 6 and 7 show, the local pressure values in the case of stronger ice seem to behave differently than in the experiments conducted by Timco (1991). In his model-scale tests, Timco only performed experiments with ice having the flexural strength up to approximately 100 kPa. If the ice strength would have been further increased, the results on the load distribution might have changed. Full-scale observations from an ice-cone interaction process (Tripathi et al., 2011), results from two-dimensional FEM-DEM simulations of ice-structure interaction against a wide inclined structure (Paavilainen and Tuhkuri, 2012), and model-scale experiments on ice interacting with a downward sloping structure (Lu et al., 2013) have also indicated that the pressures would mainly be transmitted to the waterline region. Based on the experiments here, it appears that as the rubble pile grounds and the ice is strong enough to consist of individual ice blocks, the spatial pressure distribution does not agree with previous studies. In the experiments here, however, there was a significant amount of ice rubble in front of the structure and the measured ice pressure did not associate with the intact ice sheet, as may have been with the other studies.

Local pressures during the experiments were typically concentrated in high pressure zones and a large part of the tactile sensor area seemed to be non-loaded (Fig. 6). This tendency at the instances of peak load events can be examined similarly to Frederking (2004) as follows. The peak load events were selected from the pressure records by using Rayleigh separation (Section 4.2). Table 2 shows the average number of tactile sensor sensels, N_W and N_M , subjected to loading within different pressure ranges with weak and medium ice, respectively. The total number of tactile sensor sensels was 1768. The reader should notice that the pressure ranges are here treated as relative and, thus, have no unit.

Table 2 demonstrates that the area subjected to any loading (range > 0) is approximately 50% higher with weak ice than with medium ice. However, with the medium ice, a larger number of high individual pressure values were measured (ranges with > 50). It appears that weaker ice yields lower pressure values, but the load is distributed on

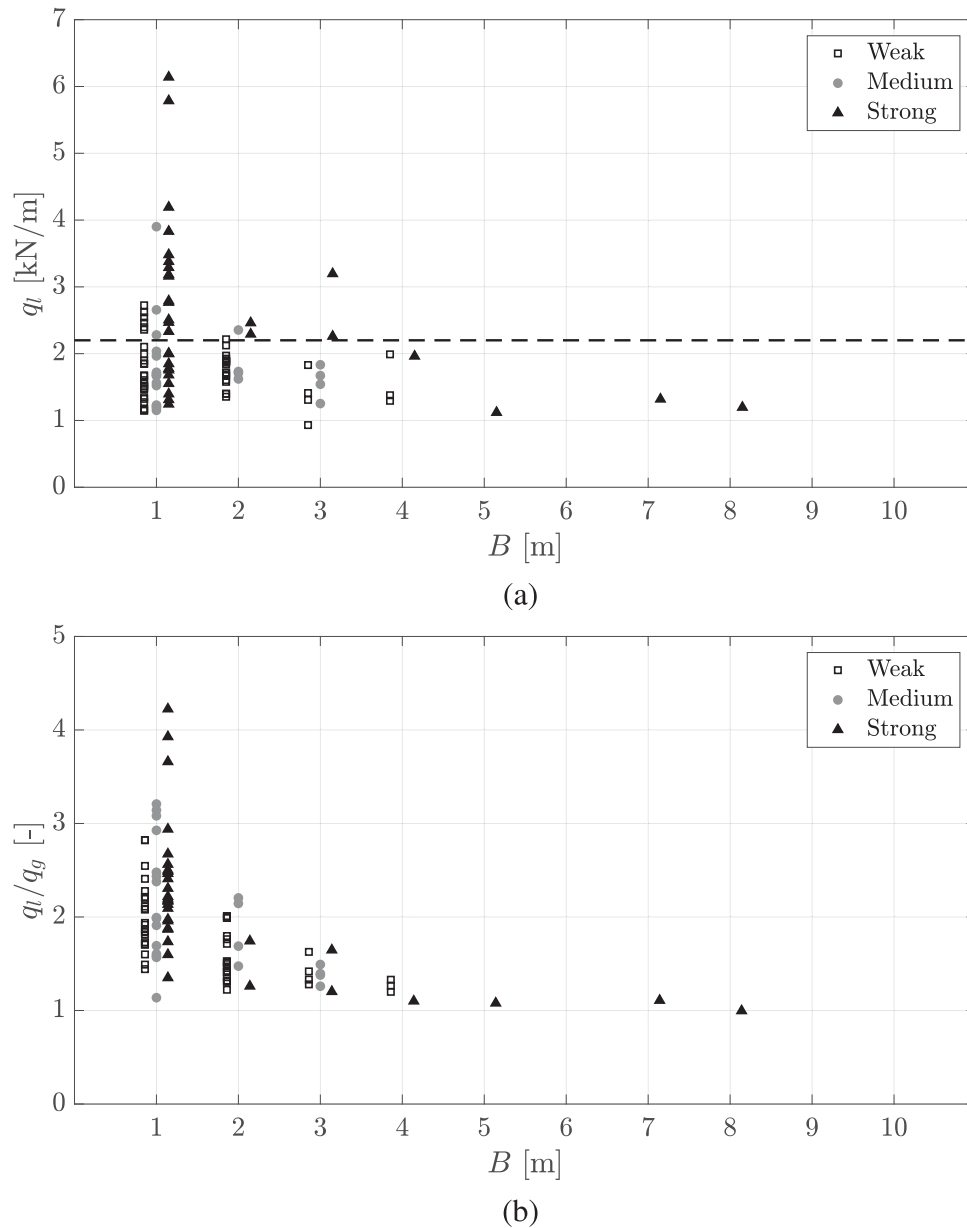


Fig. 12. (a) The line load of the load event, q_l , and (b) the ratio between q_l and the global line load, q_g , as a function of the width of the load event, B . The local line load during the highest measured global load reached a value of 2.2 kN/m, which is indicated by a dashed line in Figure (a).

a larger area, whereas the stronger ice induces large pressure peaks on smaller areas. As Lemström et al. (2022) showed, the weak ice yielded higher global loads than the medium ice. Thus, even if the local pressure values are smaller with weak than with stronger ice, the slushy morphology of the rubble piles consisting of weak ice can transfer the loads to larger areas, effectively leading to higher global loads on the structure.

5. Conclusions

This paper described model-scale experiments conducted to explore the process of level ice interacting with a wide, sloping structure in shallow water. During the experiments, an initially intact ice sheet was pushed against a ten-meter-wide structure, divided into ten identical segments along its waterline. The horizontal ice load on each segment was measured independently and, in addition, tactile sensors were utilized to measure the ice pressure on two of the segments. The

Table 2

The average amount of loaded tactile sensor sensels within different pressure ranges at the instance of the peak load events. The total number of sensels in a tactile sensor was 1768.

Pressure range	N_W	N_M	N_W/N_M
> 0	153.7	103.2	1.49
0–10	98.0	60.9	1.61
10–25	38.7	22.6	1.71
25–50	11.8	11.7	1.01
50–100	4.6	5.8	0.79
> 100	0.5	2.1	0.26

strength of the model ice was varied. The focus was on the spatial distribution of the ice load, the relationship between the loads on

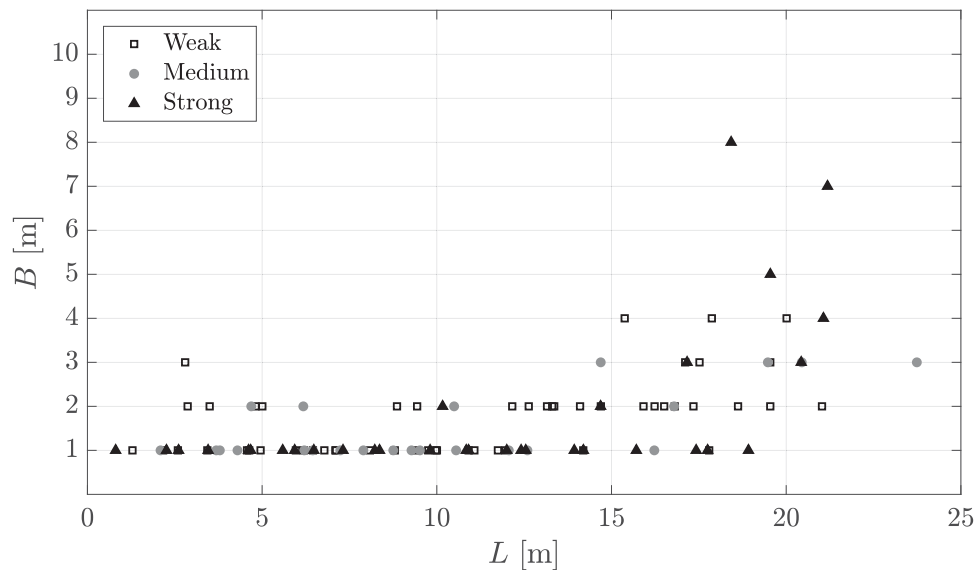


Fig. 13. The load event width, B , as a function of the length of ice pushed against the structure, L .

different segments and the correlation between global and local loads. Based on the analysis, the following conclusions are made:

- The ice load records measured on the individual segments over the whole experiment correlated strongly (Sections 3.1 and 4.1). The correlation coefficients for the load records were high and the values of the mean and the maximum loads were approximately equal for all segments. On the level of the entire interaction process, the assumption of non-simultaneous ice load does not apply.
- Despite high correlation coefficients of the complete ice load records, the ice load records of the individual segments also showed transient peaks, which could be used to define local peak load events (Section 4.2). Most of the load events were concentrated on one segment only, and very few load events covered more than three segments or 60 times the ice thickness.
- Narrow local peak load events produced the highest local line loads, with the magnitude and the share of the narrow events increasing with the ice strength. Local line loads were up to four times the magnitude of the simultaneous global line loads (Section 4.2).
- An inclined structure having the ice thickness to structure width ratio of 1:100 (width of approximately 5 m) would here have been wide enough to be considered infinitely wide in regards of high-load events (Section 4.2).
- The local ice pressure, as measured with tactile sensors, was initially more or less evenly distributed and mainly located underwater. After a grounded rubble pile had formed, the weakest ice yielded a line-like zone of high pressure at the waterline, while with the stronger ice, no high pressures were observed close to the waterline, but instead, zones of high pressure appeared at upper parts of the segments (Section 3.2).

This paper focused on the ice load distributions of the model-scale experiments. The global ice load levels, the parameter effects on the global ice load, and the mechanical phenomena during the ice loading process during the experiments are discussed in Lemström et al. (2022). This experimental campaign was conducted using a unique experimental set-up. Future work should, however, include variation in parameters, such as structure slope, ice thickness and water depth. While further model-scale tests would be beneficial, some combinations of parameters cannot for practical reasons be varied in model-scale experiments. Thus, experimental studies should be complemented

with numerical simulations similarly to Lemström et al. (2020), who used the finite-discrete element method to simulate shallow water ice-structure interaction in full-scale.

CRediT authorship contribution statement

Ida Lemström: Conceptualization, Methodology, Validation, Formal analysis, Investigation, Data curation, Writing – original draft, Visualization. **Arttu Polojärvi:** Conceptualization, Methodology, Supervision, Writing – review & editing. **Otto Puolakka:** Methodology, Writing – review & editing. **Jukka Tuhkuri:** Writing – review & editing.

Declaration of competing interest

The authors declare that they have no known competing financial interests or personal relationships that could have appeared to influence the work reported in this paper.

Acknowledgments

IL wishes to acknowledge the financial support from Alfred Kordelin Foundation, Finland, K. Albin Johanssons stiftelse, and from Aker Arctic Technology Inc., Finland and Finnish Maritime Foundation, Finland through the Industry-Academia Graduate School at Aalto University Department of Mechanical Engineering. The authors are also grateful for the financial support from Business Finland, Aker Arctic Technology Inc, Finland, ABB Marine, Finland, Arctia Shipping, Technip Offshore Finland Oy, Suomen Hyötytuuli Oy, Finland, Finnish Transport Agency, Finland and Ponvia Oy, Finland through the ARAJÄÄ research-project. The authors express their appreciation to Aalto Ice Tank staff Teemu Päiväranta and Lasse Turja for their work on the experiments.

Appendix. Reliability of tactile sensor measurements

Tactile sensors have been used in several studies related to local ice loads (Sodhi, 1998, 2001; Frederking, 2004; Gagnon, 2008a,b; Määttä et al., 2011, 2012; Serré et al., 2013a,b; Lu et al., 2013). It has been shown that obtaining accurate measurements on pressure values within a contact area is difficult, and that the measured spatial pressure distributions are highly dependent on the resolution of the sensing equipment. To assess the accuracy of the tactile sensor measurements in these experiments (Section 3.2), the loads measured by the sensors were compared to the segment load measurements. To obtain the horizontal

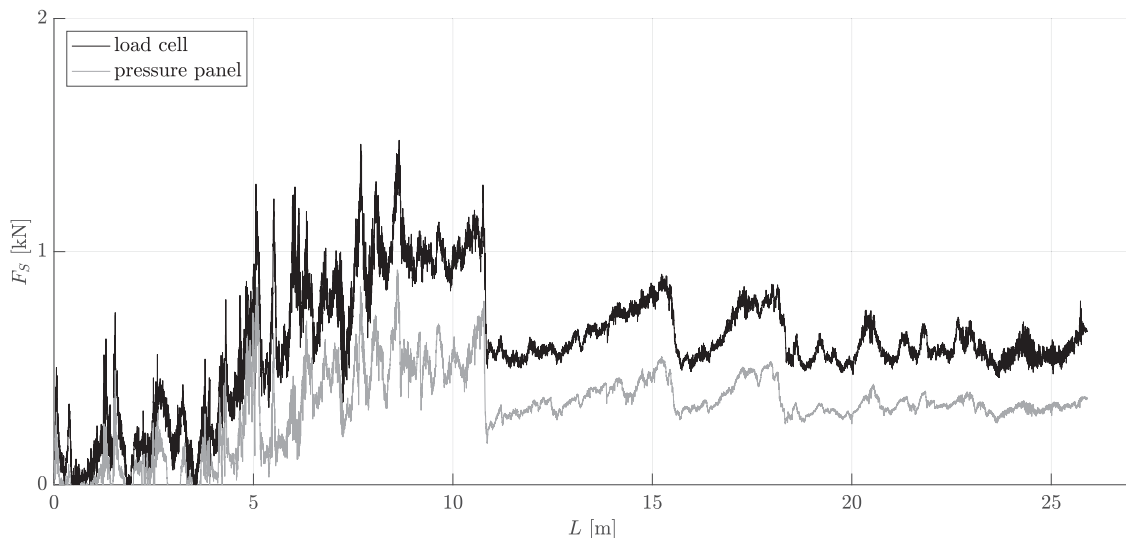


Fig. A.14. The horizontal ice load records measured by the load cell, versus the one obtained by transforming the tactile sensor measurements to force values and projecting them in the horizontal direction, as functions of the length of ice pushed against the structure, L for segment 5 of experiment M-2. The correlation coefficient between the two load records is 0.92.

load data for the sensor, the measured local pressure values were summed and integrated to a force and projected into the horizontal direction.

Fig. A.14 shows the records for the measured segment load, F_S , and the load derived for the tactile sensor. The records correlate strongly: The Pearson correlation coefficient between the data sets was 0.92. Since the tactile sensor does not cover the entire area of the segment, the load measured by it would be expected to be lower than the segment load. The ratio between the mean value of the load measured by the tactile sensor and the segment load was approximately 0.54, whereas the tactile sensor covered approximately 43% of the segment area. High correlation coefficients were observed in all experiments with successful tactile sensor measurements, which instils confidence to them.

References

- Bridges, R., Riska, K., Hopkins, M., Wei, Y., 2019. Ice interaction processes during ice encroachment. *Marine Struct.* 67, 102629.
- Bridges, R., Riska, K., Schroeder, C., 2016. Model tests for ice encroachment and formation of rubble ice. In: Proceedings of the 23rd IAHR International Symposium on Ice, Ann Arbor, Michigan, USA.
- Croasdale, K., 2011. Platform shape and ice interaction: A review. In: Proceedings of the 21st International Conference on Port and Ocean Engineering under Arctic Conditions, Montreal, Canada.
- Daley, C., Tuhkuri, J., Riska, K., 1998. The role of discrete failures in local ice loads. *Cold Reg. Sci. Technol.* 27 (3), 197–211.
- Enkvist, E., 1972. On the ice resistance encountered by ships operating in the continuous mode of ice breaking. Technical report, The Swedish Academy of Engineering Sciences in Finland.
- Evers, K., Weihrauch, A., 2004. Design and model testing of ice barriers for protection of offshore structures in shallow water during winter. In: Proceedings of the 17th IAHR International Symposium on Ice, Saint Petersburg, Russia.
- Fransson, L., 2001. Some observations of continuous and intermittent crushing failure of ice. In: Proceedings of the 16th International Conference on Port and Ocean Engineering under Arctic Conditions, Ottawa, Ontario, Canada.
- Frederking, R., 2004. Ice pressure variations during indentation. In: Proceedings of the 17th IAHR International Symposium on Ice, Saint Petersburg, Russia.
- Gagnon, R., 2008a. Analysis of data from bergy bit impacts using a novel hull-mounted external impact panel. *Cold Reg. Sci. Technol.* 52, 50–66.
- Gagnon, R., 2008. A new impact panel to study bergy bit/ship collisions. In: Proceedings of the 19th IAHR International Symposium on Ice, Vancouver, BC, Canada.
- Hyunwook, K., Daley, C., Colbourne, B., 2018. A study on the evaluation of ice loads and pressure distribution using pressure indicating film in ice-structure interaction. *Ocean Eng.* 165, 77–90.
- Jordaan, I., 2001. Mechanics of ice-structure interaction. *Eng. Fract. Mech.* 68, 1923–1960.
- Karulin, E., Karulina, M., Blagovidov, L., 2007. Ice model tests of caisson platform in shallow water. *Int. J. Offshore Polar Eng.* 17, 270–275.
- Lemström, I., Polojärvi, A., Tuhkuri, J., 2020. Numerical experiments on ice-structure interaction in shallow water. *Cold Reg. Sci. Technol.* 176, 103088.
- Lemström, I., Polojärvi, A., Tuhkuri, J., 2022. Model-scale tests on ice-structure interaction in shallow water: Global ice loads and the ice loading process. *Marine Struct.* 81, 103106.
- Lu, W., Serré, N., Høyland, K., Evers, K., 2013. Rubble ice transport on Arctic offshore structures (RITAS), part IV: Tactile sensor measurement of the level ice load on inclined plate. In: Proceedings of the 22nd International Conference on Port and Ocean Engineering under Arctic Conditions, Espoo, Finland.
- Määttänen, M., Løset, S., Metrikine, A., Evers, K., Hendrikse, H., Lønøy, H., Metrikin, I., Torodd, N., Sergiy, S., 2012. Novel ice induced vibration testing in a large-scale facility: deciphering ice induced vibrations, part 1. In: Proceedings of the 21st IAHR International Symposium on Ice, Dalian, China.
- Määttänen, M., Marjavaara, P., Saarinen, S., Laakso, M., 2011. Ice crushing tests with variable structural flexibility. *Cold Reg. Sci. Technol.* 67, 120–128.
- Paavilainen, J., Tuhkuri, J., 2012. Parameter effects on simulated ice rubbing forces on a wide sloping structure. *Cold Reg. Sci. Technol.* 81, 1–10.
- Palmer, A., Croasdale, K., 2013. *Arctic Offshore Engineering*. World Scientific Publishing Co. Pte. Ltd., Singapore, pp. 225–229.
- Repetto-Llamarez, A., Gürtner, A., Gumestad, O., Høyland, K., 2009. Qualitative description of a should ice barrier-ice interaction during model tests. In: Proceedings of the ASME 28th International Conference on Ocean, Offshore and Arctic Engineering, Honolulu, Hawaii.
- Repetto-Llamarez, A., Gudmestad, O., Gürtner, A., Gumestad, O., Høyland, K., 2009. Shoulder ice barrier ice tank testing part II: Estimation of breaking length and block size using image analysis. In: Proceedings of the ASME 28th International Conference on Ocean, Offshore and Arctic Engineering, Honolulu, Hawaii.
- Riska, K., Uto, S., Tuhkuri, J., 2002. Pressure distribution and response of multiple panels under ice loading. *Cold Reg. Sci. Technol.* 34, 209–225.
- Serré, N., Høyland, K., Lundamo, T., Bonnemaire, B., Evers, K., Gürtner, A., 2013. Rubble ice transport on Arctic offshore structures (RITAS), part I: Scale-model investigations of level ice action mechanisms. In: Proceedings of the 22nd International Conference on Port and Ocean Engineering under Arctic Conditions, Espoo, Finland.
- Serré, N., Lu, W., Høyland, K., Bonnemaire, B., Borge, J., Evers, K., 2013. Rubble ice transport on Arctic offshore structures (RITAS), part II: 2D Scale-model study of the level ice action. In: Proceedings of the 22nd International Conference on Port and Ocean Engineering under Arctic Conditions, Espoo, Finland.
- Sodhi, D., 1998. Nonsimultaneous crushing during edge indentation of freshwater ice sheet. *Cold Reg. Sci. Technol.* 27, 179–195.
- Sodhi, D., 2001. Crushing failure during ice-structure interaction. *Eng. Fract. Mech.* 68, 1889–1921.
- Suominen, M., Kujala, P., Romanoff, J., Remes, H., 2017. Influence of load length on short-term ice load statistics in full-scale. *Marine Struct.* 52, 153–172.
- Timco, G., 1991. The vertical pressure distribution on structures subjected to rubble-forming ice. In: Proceedings of the 11th International Conference on Port and Ocean Engineering under Arctic Conditions, St. Johns, Canada, pp. 185–197.
- Timco, G., Sayed, M., Frederking, R., 1989. Model tests of load transmission through grounded ice rubble. In: 8th International Conference on Offshore Mechanics and Arctic Engineering, The Hague, Netherlands, volume 1, pp. 269–274.

- Tripathi, D., Mayne, D., Brown, T., 2011. Detailed pressure distribution analysis of a Confederation Bridge pier. In: Proceedings of the 21st International Conference on Port and Ocean Engineering under Arctic Conditions, Montreal, Canada.
- Valanto, P., 2001. The resistance of ships in level ice. In: SNAME Transactions 119, pp. 53–83.
- Varsta, P., Riska, K., 1977. Failure Process of ice edge caused by impact with a ship's side. In: Ice ships in winter navigation, Symposium in Oulu University, Oulu, Finland.
- Yoshimura, N., Inoue, M., 1985. Model tests of ice rubble field around a gravel island. In: Proceedings of the 8th International Conference on Port and Ocean Engineering under Arctic Conditions, Narssarsuaq, Greenland pp. 716–726.